Numerical/experimental strategies to infer enhanced liquid thermal conductivity and roughness in laser powder-bed fusion processes

S. Ancellotti[1*], V. Fontanari[1], A. Molinari[1], E. Iacob[2], P. Bellutti[2], V. Luchin[3], G. Zappini[3], M. Benedetti[1]

[1]Department of Industrial Engineering, University of Trento, Via Sommarive 9, 38123 Trento, Italy

[2]Center for Materials and Microsystems, Fondazione Bruno Kessler (FBK), Via Sommarive, 18, 38123, Povo (TN), Italy

[3] Eurocoating spa, Via Al Dos de la Roda, 60, 38057 Ciré-Pergine (TN), Italy

*Contacting Author:

Simone Ancellotti

Tel. +390461282457

Fax +390461281977

E-mail: simone.ancellotti@unitn.it

Abstract

Modelling the thermal behaviour of the melt pool produced in Laser Powder-Bed Fusion (L-PBF) processes is not an easy task, as many complex non-linear thermal phenomena are involved. An effective way to make the computational cost of these analyses affordable is to model powder and molten metal as continuous media, wherein all the heat transfer modes occurring in the liquid are simulated as lumped fictitious heat conduction. The augmentation factor used to enhance the thermal conductivity of the liquid is in general calibrated through experimental estimations of the melt pool size. The present work is aimed at devising a robust method for the calibration of such thermal parameters. A specific point of novelty of the present paper is the definition of a method to correlate surface roughness and numerically predicted melting pool size. This strategy is able to predict with good accuracy the roughness of L-PBF fabricated parts and could pave the way for calibration strategies based on roughness measurements. For this purpose, a 3-factor, 3-level Design of Experiment (DoE) has been carried out to investigate melting pool size and roughness by changing the machine process parameters: laser power, hatch distance, time exposure. In this way, the calibration of the thermal properties is made less sensitive to the large uncertainty usually affecting the melt pool size measurements and the range of applicability of the thermal model is explored over a broad spectrum of L-PBF process parameters.

Anisotropic and isotropic enhanced thermal conductivity approaches are applied in combination with a laser source modelled either as a 2D or 3D heat source, respectively. <mark>The latter approach proved to be more accurate and robust against experimental uncertainties.</mark>

Keywords: Laser Powder-Bed Fusion, Additive manufacturing, Ti-6Al-4V, Finite element; thermal model, melting pool size, single scanning seam, roughness, enhanced thermal conductivity;

1. Introduction

Additive manufacturing (AM) technologies are making a huge impact on the industrial context, as very complex shaped parts can be manufactured in a reasonable time. Among them, Laser Powder Bed Fusion (L-PBF) is currently the most utilized, since it can work with a wide range of metallic materials [1]. Specifically, a focused laser beam moving according to a predetermined path induces a selective cohesion of grains of a deposited powder layer, thus generating a slice of the component. In this way, the part is built slice-by-slice. In particular, the cohesion is achieved in L-PBF through melting of powder particles in a similar manner of welding [1]. Despite this simple concept, fabricating a part via L-PBF with satisfactory geometrical accuracy and adequate mechanical properties is not straightforward, as these aspects are dictated by an intricate plethora of process parameters, such as material properties, powder characteristics, laser intensity, scanning strategy, process kinematics [2]. Their interplay is not yet fully understood and is currently matter of intensive research in both academic and industrial field. Special emphasis is placed on the identification of a suitable space of process parameters, within which defects, such as residual stresses, porosity and surface balling, are minimized [3-8]. Until now, the identification of the optimal process parameters was mainly achieved through expensive trial and error approaches. More recently, numerical modelling emerged as a valid alternative to investigate the phenomena involved in L-PBF.

L-PBF modelling approaches can be categorized in micro/mesoscopic and macroscopic models. These last models were mainly developed for predicting residual stresses in a macroscopic component with an affordable computational cost, but neglecting the physics of the L-PBF process at the microscopic scale [5]. Several strategies were employed to increase the computation efficiency of such simulations, among them element birth-and-death [9,10], Cholesky decomposition [11], adaptive mesh refinement [12,13]. Despite these improvements, the computation time of macroscopic models with elements smaller than laser spot remains still too high, even for simulating the manufacturing of small components; for instance, simulating all the laser spots lying on few thousand layers may take two weeks or longer [14]. This problem can be partially solved with an analytical solution of the thermal field after the laser scanning [15]. This approach, however, gives only the global temperature field of a single layer without distinguishing the heat

distribution due to the multiple scanning strategies. Thus, for the sake of simplicity, macroscopic-scale approaches at layer- or part-level have been proposed. Papadakis et al. [16] proposed a more approximated volume-by-volume method. Instead of simulating each spot interaction, three layers are simultaneously molten by inducing volumetric generated heat. Denlinger et al. [17] minimised the degrees of freedom of their model by coarsening the mesh sub-layers. The upper layer having finer mesh is merged to the lower layers. Stathatos et al. [18], taking inspiration from Hu et al. [19], devised a fully parametric FE model of L-PBF discretizing the powder bed with thermal shell elements instead of solid elements. This strategy significantly reduced the computational heaviness and the results were in very good agreement with those published in many works [20]. Ganeriwala [21] devised a discrete element approach, in which the powder particles are modelled as discrete spheres, interacting to each other and with the substrate, and mechanical contact and thermal transmission are considered. Yang et al. [22] extended and implemented the approaches developed for the simulation of the welding process. They tried two different heat-source models: line heat-source model and layer heating model. The first one approximates the laser scan as a heat flux along a heat line, whereas, in the second one, few layers are melted together. They concluded that residual stress and deformation depend on the structure stiffness, that line-heating model is not adequate to simulate large parts, whereas the layer-heating method seems more promising.

Such macroscopic numerical models are particularly suitable when residual stresses at the component scale must be predicted to reduce distortions and optimize supporting structures. However, if other sources of defectiveness are of interest, like lack-of-fusion-defects and surface roughness, numerical analyses at the scale of the melting pool are necessary. In this case, the analyses are usually restricted to small portions of the component, involving few laser scans, due to the extremely fine mesh size and the large number of time steps required to capture the numerous nonlinear physical phenomena involved in the L-PBF process, like convective heat, liquid flow and laser/matter interactions. To this regard, Marangoni convection has been demonstrated to influence the melting pool profile and temperature distribution [23]. Unfortunately, the analysis of such phenomenon requires complicated computational fluid dynamics (CFD) simulations. To overcome this problem, Safdar [24] proposed a method called isotropic enhanced thermal conductivity for continuous medium solid models, wherein the molten material is still treated as a continuum, yet with different temperature-dependent material properties, and the thermal conductivity is fictitiously augmented by a factor λ to account for the additional heat flow transmitted via Marangoni convection. The value of λ is indirectly deduced from experimental data, for instance from the size of the melt pool determined through dedicated experimental campaigns. As a result, continuous medium models can be calibrated to simulate the realistic heat transfer of melting pool without considering the liquid flow. Later, the same authors [25] refined their approach and demonstrated that "anisotropic enhanced thermal conductivity" is more accurate. But, many researchers prefer using the isotropic approach to reduce

computation time at the expense of accuracy. For instance, Ali et al. [26] found λ equal to 4 for L-PBF of Ti-6Al-4V with trial and error tests. The choice between isotropic and anisotropic approaches is still debated and the effective value of calibration for λ is not yet clear and depends on many factors.

Another issue involved in the analysis of the melt pool behavior is the laser/powder interaction. In the literature, this is usually modelled as a heat source according to different approaches originally devised for simulating the laser welding process. To this regard, Rosenthal et al. [27] proposed an analytical solution for a point heat source, traveling in a 1D space. Later, Eagar and Tsai [28] developed an analytical model of a moving heat source having a 2D Gaussian spatial distribution. Then, Goldak et al. [29] proposed a 3D heat source model with double-ellipsoidal distribution. These approaches were then applied for the thermal modelling of powder bed-based AM processes. The majority of published papers in the open technical literature [30-36] models the laser as a 2D heat source for the sake of simplicity and computational lightness, though some scholars [21, 37-40] are of the opinion that laser beam heating is more accurately predicted by 3D heat source models. However, this would raise the question on the actual penetration depth of the laser into the powder bed, which depends on material, powder granulometry and geometry and how this may be modelled. Fischer et al. [41] found that laser penetration could be around 60 μm for commercially pure titanium powder and this value was assumed by Ali et al. [26] to model the laser influence as a volumetric heat generation. Anyway, the depth-distribution of laser irradiance to be set in the model is still debated and, up to now, is based on preliminary assumptions only.

Aim of the present work is to compare different modelling strategies to efficiently perform thermal analyses at the microscopic scale and to devise several experimental approaches for fine-tuning of the thermal properties to be input into the numerical models. Specifically, both anisotropic and isotropic enhanced thermal conductivity approaches will be evaluated in combination with a laser source modelled either as a 2D or 3D heat source, respectively. The thermal properties, i.e. enhancement factor λ and laser penetration depth, are deduced from experimental measures of the melt pool size. For this purpose, a 3-factor, 3-level Design of Experiment (DoE) is conducted using a Renishaw L-PBF machine employing a pulsed laser beam irradiating a Ti-6Al-4V powder bed. The DoE factors are the following machine process parameters: laser power, hatch distance, time exposure. Width and height of the laser scans are evaluated using a scanning electron microscope (SEM) and a 3D contact profiler. In contrast to the majority of the papers published so far, wherein the thermal properties are calibrated from a single set of L-PBF machine parameters, a more robust calibration is here performed considering the outcomes of 27 DoE experiments. Another point of novelty of the present paper is the experimental analysis of the surface topology of macroscopic pieces fabricated via L-PBF and the analysis of the correlation between experimentally determined 3D roughness and numerically estimated size of the melt pool. This could yield a new tool for predicting the roughness of additively manufactured components and an

alternative and simpler way for calibrating the thermal properties not necessitating a dedicated testing campaign based on single laser scans.

2. Basic idea

In this work, two different modelling approaches have been devised to perform thermal analyses at the microscopic scale. The thermal properties of the model are tuned on the basis of measurements of both melting pool size and of the as-build surface morphology. The first approach, termed AETC2D, consists in simulating the powder-laser interaction as a superficial incoming thermal flux with Gaussian spatial distribution along with the implementation of an anisotropic enhanced thermal conductivity (see Fig. 1). Specifically, the unknown thermal behaviour of the liquid phase is modelled as pure heat conduction, wherein the anisotropic conductivity coefficients are assessed by augmenting the conductivity of the liquid phase by the enhancement coefficients $\lambda_x = \lambda_y$ and λ_z. These latter are calibrated so as to minimize the mean squared error in the melt pool size estimation. In the second approach IETC3D, which assumes the laser beam to be able to penetrate into the powder bed, the laser is modelled as a 3D volumetric-generated heat in a cylindrical volume, embedded in the sub-superficial region, having the radius of the laser spot and of unknown height z_{laser} to be calibrated along with the isotropic enhancement coefficient of the powder ($\lambda_x = \lambda_y = \lambda_z$). In this case, the same calibration is carried out by varying two parameters: λ and z_{laser} (see Fig. 1). More details on FE model will be provided in Sec. 4.

Basically, the model has different parameters related to the process conditions, such as point distance, dwell time, laser power, laser spot radius, chamber temperature, etc. Among them, only the first three ones are investigated since they manifest, intuitively, the major impact on the final surface morphology as reported also in the literature [2-4]. This justifies a 3-factor 3-level Design of Experiment (DoE) in the experimental campaign in order to make the model calibration more robust. Also the scanning strategy has an impact on the final morphology but it is not implemented in the model as only a short scanning line is simulated and, thus, its effect is not studied.

3. Experimental procedure

3.1. Apparatus and process parameters

The L-PBF machine utilized in this work is a Renishaw® model AM500. It operates with moving pulsating laser, whose spot radius is 35μm. Samples are fabricated using an atomized powder of Ti-6Al-4V alloy. The powder particles of approximately spherical shape have diameter comprised in the range 15-45 μm. The thickness of each deposited layer is set to 60μm.The working chamber is filled with argon to prevent powder oxidation and degradation of the powder. The internal temperature is close-loop controlled and kept at 130°C in order to minimize the energy requested

by the laser for the fusion and to avoid detrimental effects of premature warping caused by non-uniform thermal expansion (curling). Moreover, the plate base is heated to maintain both powder and manufactured component at the target temperature. The "stripe" scanning path is rotated at each subsequent layer to balance the entire temperature field. Such rotation is set equal to 67°, so that the same scanning path is repeated every 180 layers. Other important process parameters, applied in these experiments, are listed in Tab. 1. Coupons are fabricated according to a full 3-level DoE factorial plane considering the following factors: "laser power", "point distance" and "time exposure". Interestingly, the point distance is set up to three times larger than the laser spot size, because, according to our experience, the related laser input energy is high enough to create at least partially overlapped melt pools. All the 27 combinations of these three process parameters are listed in Tab. 2. All the printed samples do not undergo a post-process stress-relief treatment, as this post-procedure is not modelled in this work. Samples are built both in form of cubic blocks of 15 mm side for surface morphology analyses and in form of single scan seams. These latter were devised to get information about width and height of the melt pool necessary to calibrate the thermal numerical model. For this purpose, 2-mm-long single lines are melted in a powder bed deposited on an as-build basement that is manufactured with standard parameters of the L-PBF machine with laser power equal to 200W.

Tab. 1. Process parameters used to fabricate the sampes;

Process Parameters	
Laser power [W]	400-450-500
Point distance [μm]	70-90-110
Time exposure [μs]	40-50-60
Hatch distance [μm]	100
Layer thickness [μm]	60
Path rotation [°]	67°
Scanning strategy	Stripes

Tab. 2. Combinations of process parameters for the 27 DoE tests.

Combination	Point Distance (μm)	Time of Exposure (μs)	Laser Power (W)	Scan Speed (mm/s)	Energy Density (J/mm3)
1	70	40	400	1750	38.1
2	70	40	450	1750	42.9
3	70	40	500	1750	47.6
4	70	50	400	1400	47.6
5	70	50	450	1400	53.6
6	70	50	500	1400	59.5
7	70	60	400	1167	57.1
8	70	60	450	1167	64.3
9	70	60	500	1167	71.4
10	90	40	400	2250	29.6
11	90	40	450	2250	33.3
12	90	40	500	2250	37.0
13	90	50	400	1800	37.0
14	90	50	450	1800	41.7
15	90	50	500	1800	46.3
16	90	60	400	1500	44.4

17	90	60	450	1500	50.0
18	90	60	500	1500	55.6
19	110	40	400	2750	24.2
20	110	40	450	2750	27.3
21	110	40	500	2750	30.3
22	110	50	400	2200	30.3
23	110	50	450	2200	34.1
24	110	50	500	2200	37.9
25	110	60	400	1833	36.4
26	110	60	450	1833	40.9
27	110	60	500	1833	45.5

3.2. Surface morphology analyses

The width and the height of the cross section of each seam, taken as representative of the melt pool dimensions, are evaluated using a JEOL JSM-IT300LV scanning electron microscope (SEM), as shown in Fig. 2. Micrographs of the seams taken from the top-view are analysed by an ad-hoc MatLab script based on the image segmentation algorithm named "watershed" [42]. It distinguishes the single seams from the background surface and measures their width of each cross section with a resolution of 4µm. In addition, the 3D profile of each seam in an area of 1x0.5mm, with a sampling grid of 2.5x3µm, is acquired with a 3D Surface profiler, described in the following, in order to estimate the height. Width and height of each seam are measured along the seam-length of 2 mm at cross-sections equally spaced of 4 µm.

The surface morphology of the cubic samples is evaluated on a square area of 1 mm side, using a highly sensitive mechanical surface profiler KLA-TENCOR P6 depicted in Fig. 3a. The profiler performs 3µm-spaced linear scansions parallel to the X axis with a 2.5µm acquisition step. The acquired heights are normalized with respect to the mean 3D plane extrapolated with polynomial regression of unit degree (LOESS fitting). Looking at Fig. 3a and b, the weld tracks are clearly distinguishable and their direction is perpendicular to the X-axis.

The spatters, highlighted in red, are not- or partially melted powder grains, agglomerates of particles, or droplets of liquid material "erupted" from melting pool [43,44]. The size and shape of these spatters are intimately related to the manufacturing process parameters and the properties of the original particles. Furthermore, their presence is likely to negatively affect the accuracy in estimating the roughness parameters. As a solution, a spatter identification algorithm has been developed, following the guidance proposed by Senin et al. [45] and illustrated in Fig. 3c-h. Specifically, the spatters can be identified as protrusions from the surrounding surface, as shown in Fig. 3c. Since the spatters lie on an irregular waved surface, a discrimination based on the absolute height is not possible. Thus, 3D Gaussian high-pass filter with 18 µm cut-off is applied to damp the waviness related to the weld tracks and to highlight these protrusions. See Fig. 3d. Successively, the function "imfindcircles", implemented in MatLab, searches the protrusions with almost

circular contours, which are more likely to be spatters, as shown in Fig. 3e. Once these have been identified (Fig. 3f), they are removed from the surface (Fig. 3g) and the left void regions are reconstructed with a weighted second grade interpolation of the surface shape in the neighbourhoods (Fig. 3h). The resulting surface is smoother (without these defects) and more suitable to evaluate the roughness. The profile parameter Rq (Root mean square deviation) is used to assess the roughness and is defined by this equation defined by ISO 4287 [46]:

$$R_q = \sqrt{\frac{1}{l}\int_0^l Z^2(x)\,dx} \tag{1}$$

where l is length of the profile, Z is the height, x is the profile coordinate. As prescribed by the standard ISO 13565 [47], such parameter is calculated only on profiles conveniently filtered via Gaussian filter with cut-off wavelength 8.75 µm to suppress the longwave component. In this way, it is possible to identify the weld tracks (regarded as micro-roughness) and eliminate the waviness produced by global irregularities, as shown in Fig. 4. To take into account the variability of Rq measured on several profiles of the scanned surface, the average and the standard deviation of Rq is calculated from the corresponding values assessed by each line-scansion.

4. Modelling strategy

The FE thermal model developed in this work simulates the scan of the pulsating laser interacting with the deposited powder bed, in order to model the melting behaviour. Two different approaches have been used for modelling. The first one is based on an *anisotropic enhanced thermal conductivity* with laser interaction modelled as an imposed surface heat flux (AETC2D). The second one consists of implementing *isotropic enhanced thermal conductivity* and modelling laser irradiance as a volumetric generated heat (3D distribution) (IETC3D). The laser path is modelled as a single line composed of 15 adjacent laser spots so as to have a stabilized melting pool. The model is set in ANSYS® employing isoparametric hexahedral 8-node brick elements SOLID70. Though the powder-bed-behaviour is quite complex due to presence of grains, it is approximated as a continuum for the sake of computational lightness, as shown in Fig. 5. The powder bed, having size 2x0.4mm and thickness 60µm, is deposited on a substrate, representing the base plate, whose height is 0.2 mm. These dimensions have been conveniently studied so as to minimize the boundary effects on the melting pool size, in order to reproduce a more realistic situation, in which the portion of involved material is small in comparison to the macro-scale dimension of a real powder bed. A convergence analysis to validate the mesh size has been carried exploring mesh sizes down to 6µm. An element size of 10µm has been found to be an adequate compromise between accuracy and computational time. The mesh is refined in the vicinity of the melt pool becomes coarser moving away from it, so as to reduce the computation cost.

The heat transfer is governed by the following equation:

$$\left(K_x \frac{\partial T}{\partial x} + K_y \frac{\partial T}{\partial y} + K_z \frac{\partial T}{\partial z} \right) + Q = \rho C_p \frac{\partial T}{\partial t}$$

(2)

where T is the temperature, t is the time; x, y and z are spatial coordinates; K_x, K_y and K_z are the thermal conductivities along the x-, y- and z-direction, respectively. ρ is the density; C_p is the specific heat and Q is the heat source term.

4.1. Heat source

The laser interaction can be approximated as an imposed heat flux on a surface or as a volumetric thermal load. In this study, both approaches have been adopted. For the 2D laser distribution, the heat source is modelled as a 2D superficial heat flux applied on the surface of the powder bed moving according to a line. The laser irradiance distribution, described by Eq. (3), in each laser spot is assumed Gaussian dependent to the radial distance r from the centre of the spot.

$$I = \frac{2AP}{\pi r_{max}^2} e^{\left(-2 \frac{r^2}{r_{max}^2} \right)}$$

(3)

Where A is powder absorbance, P is laser power and r_{max} is laser beam radius, which is equal to 35µm.

For the 3D laser distribution, the laser is modelled as a volumetric heat generated in a cylindrical volume of height z_{laser}, as indicated by Eq. (4). The Gaussian distribution with respect to radial distance r from the spot centre (Eq. (3)) is kept, but is distributed uniformly along the depth z.

$$I = \begin{cases} \dfrac{2AP}{\pi r_{max}^2} e^{\left(-2 \frac{r^2}{r_{max}^2} \right)} \dfrac{1}{z_{laser}} & \text{for } 0 \leq z < z_{laser} \\ 0 & z \geq z_{laser} \end{cases}$$

(4)

4.2. Initial conditions and boundary conditions

The L-PBF process is carried out in controlled close-loop atmosphere at 130°C. Thus, this temperature is set as initial condition of all the nodes of the model. Since the working chamber is filled with argon to prevent powder oxidation, natural convection is applied on the top surface, except for the top surface where the heat flux of laser is imposed. Since introducing the emitting radiation flux increases the non-linearity of the analysis, this aspect was not considered. As a solution, we used an empirical relationship, proposed in [48,49], combining the effect of both radiation and convection into a lumped heat transfer coefficient. In view of the low value of thermal conductivity expected for powder, adiabatic behaviour is considered on the lateral surfaces (no heat flux is permitted). Bottom nodes are constrained with imposed temperature of 130°C, in order to imitate the thermal inertia of the entire bulk material of the base plate, which is

preheated at this temperature. To reduce the number of nodes, boundary condition of symmetry is imposed on the lateral plane passing through the axis of the laser scanning line.

4.3. Material properties

In view of the numerous non-linear phenomena, such as phase-transition, melting, cooling, solidification, and vaporization occurring during L-PBF, the material properties in the model must be temperature dependent. The phase-transition is defined by the enthalpy curves for powder and solid, which consider the latent heat. The material properties are extracted from the literature [50,51] and are valid for the solid bulk state. Conversely, the powder properties are simplified according to the following assumptions. Powder density and thermal conductivity are assumed to be 60% and 10% of those of the solid material, respectively. See Tab. 3, 4, 5 and Fig. 7.

Tab. 3. Variation of thermal conductivity with temperature;

Thermal Conductivity [W/mK]		
Temperature [°C]	Solid	Powder
0	6.1874	0.6187
19	6.5660	0.6566
399	12.2620	1.2262
800	18.1490	1.8149
1198	23.4590	2.3459
1499	27.8010	2.7801
1605	29.9134	2.9913
1660	14.9567	14.9567
3265	14.9567	14.9567
3295	7.4784	7.4784
5000	7.4784	7.4784

Tab. 4. Thermal parameters;

Thermal parameters	Solid	Powder
Density [kg/m^3]	4220	2532
Solidus temp [°C]	1605	1605
Liquidus temp [°C]	1660	1660
Vapour temp [°C]	3265	3265
Saturation temp [°C]	3295	3295
Specific heat for solid [J/kgK]	708.8	708.8
Specific heat for liquid [J/kgK]	1000	1000
Specific heat for vapour [J/kgK]	1500	1500
Latent heat of fusion [J/kg]	365000	365000
Latent heat of vapour [J/kg]	9376200	9376200

Tab. 5. Variation of enthalpy with temperature.;

Enthalpy [J/m^3]		
Temperature [°C]	Solid	Powder
0	0	0
1605	4.8008e+9	2.8805e+9
1660	6.5398e+9	6.5398e+9
3265	1.3312e+10	1.3312e+10

3295	1.4210e+10	1.4210e+10
5000	6.5237e+10	6.5237e+10

Looking at Fig. 6, it can be noticed that the enthalpy and thermal conductivity curves of powder and solid are coincident only above the melting point. When the average nodal temperature of an element exceeds the melting point, the element is considered completely molten and the corresponding liquid material properties are assigned. After solidification, which is considered to occur when the average nodal temperature drops below the melting point, the solid material properties are implemented. Obviously, this process is irreversible.

The thermal conductivity is defined also in the liquid and vapour phase and, as a first attempt, it is set as the half of the value at the transition point. We are aware that these assumptions are not supported by empirical evidences, even because the actual value of the thermal conductivity above the melting point is still unknown. Nevertheless, we believe these assumptions to be reasonable for a first attempt to the problem and their acceptability will be evaluated through comparison of the numerical estimations with the outcomes of experimental measurements. The heat transmission of the melting pool is further complicated by numerous physical phenomena such as liquid convection, radiation, depression, wetting and etc. In particular, the Marangoni convection has been proven to amplify remarkably the heat-transfer of the liquefied metal [52]. In this paper, the thermal behaviour is modelled in a simplified manner, whereby all the aforementioned heat transmission modes are simulated as a fictitious thermal conduction. The corresponding thermal conductivity of the liquid phase (thus above the melting point) is calibrated in order to make the predictions of the FE model in terms of melt pool size in accord with experimental measures. More specifically, two approaches, both relying on the calibration of two unknown parameters, are adopted. In the former one, the enhanced thermal conductivity is considered to be orthotropic, wherein the in-plane values K'_x and K'_y are assumed to be equal and augmented by a factor λ_x with respect to the baseline conductivity K. The out-of-plane conductivity K'_z is instead enhanced by a factor λ_z.

$$K'_x = K'_y = \lambda_x \cdot K$$
$$K'_z = \lambda_z \cdot K$$
(5a)

The laser is in this case modelled as a 2D superficial heat flux (Eq. (3)).

In the latter approach, the enhanced thermal conductivity is considered to be isotropic and assumed to be augmented in all the directions by the same enhancement factor λ:

$$K'_x = K'_y = K'_z = \lambda \cdot K$$
(5b)

The laser is in this case modelled as a 3D heat generation (Eq. (4)), wherein the depth of the volume interested by heat generation is the second unknown parameter to be calibrated.

4.4. Estimating the surface roughness from the thermal model

Looking at the surface profiles illustrated in Fig. 2 and 3a, it is evident that the surface morphology produced by L-PBF consists essentially in a wavy pattern and, to a smaller length scale, in a random distribution of surface defects in the form of spatters and droplets. While it is hard to find a correlation between these latter features and the thermal behavior simulated by the present FE model, it is reasonable to argue that the surface waviness is the result of the sequential superstition of the seams created during the laser scans. This scenario is schematically illustrated in Fig. 7: two adjacent seams of idealized semi-elliptical shape are spaced apart by the hatch distance, and thus partially overlapped. The upper profile (dashed red line) of the Boolean addition of the two areas represents the ideal linescan profile of the 3D printed surface. If we assume that height and width of the semi-elliptical seams are well represented by the corresponding sizes of the melt pool, thus neglecting the alterations produced by successive laser scans, it is possible to estimate from Eq. (1) the waviness contribution to the surface roughness from the outcomes of the thermal FE simulations. The reasonability of such approach is confirmed by Fig. 8, which plots the Rq roughness estimated from the experimental measures of melt pool width and height vs. the experimental measures of Rq. Although affected by large uncertainty, the plot indicates a clear correlation between estimated and measured values of Rq. This promising outcome stimulated the investigations shown in the following aimed at identifying a possible correlation between the experimental measures of Rq and its predictions based on numerical estimations of melt pool width and height.

4.5. Calibration procedure

The calibration of the bi-parametric thermal FE models is performed by least-square fitting the experimental measures of melt pool width and height obtained from the weld seams fabricated according to the DoE illustrated in Table 2. A notable advantage of this procedure is that the optimal values of the FE parameters are obtained under diverse combinations of the L-PBF machine operating conditions, thus offering a versatile numerical tool for the investigation of thermal behaviour and a robust calibration of the parameter, being this a critical issue given the high uncertainty affecting the experimental determination of the melt pool dimension. Specifically, the best-fit parameters are obtained through minimization of the following weighted sum of square residuals:

$$\varepsilon_w = \sum_{i=1}^{n} \frac{\left(w_i^{FEM} - w_i^{\exp}\right)^2}{std\left(w_i^{\exp}\right)}$$

$$\varepsilon_h = \sum_{i=1}^{n} \frac{\left(h_i^{FEM} - h_i^{\exp}\right)^2}{std\left(h_i^{\exp}\right)} \tag{6}$$

$$\varepsilon_{w,h} = \varepsilon_w + \varepsilon_h$$

where n is the number of data (27 in the present case), w_i and h_i are width and height of the weld seam produced by the i-th experiment listed in Table 2. "std" denotes the standard deviation of the experimental measures. The superscripts "FEM" and "exp" indicate the numerical and experimental value, respectively.

As additional index of the goodness of the fitting procedure, the following weighted sum of square residuals will be used:

$$\varepsilon_{Rq} = \sum_{i=1}^{n} \frac{\left(Rq_i^{FEM} - Rq_i^{\exp}\right)^2}{std\left(Rq_i^{\exp}\right)} \tag{7}$$

where Rq_i represents the average Rq roughness parameter measured on the i-th sample. Again, "std" denotes the standard deviation of the experimental measures. The superscripts "FEM" and "exp" indicate the numerical and experimental value, respectively. The former is calculated as described in Fig. 7, the latter is estimated according to Eq. (1).

The uncertainty on the FE thermal parameters estimation is assessed according to the Monte Carlo method. For this purpose, 1,000 trials are considered. In each trial, a population of melt pool size and roughness data is randomly generated assuming a Gaussian probability density function with mean and standard deviation given by the experimental measures. For each trial, the thermal parameters are calculated searching for the minimization of either $\varepsilon_{w,h}$ or ε_{rough}. For this purpose, response curves, some of them exemplarily shown in Fig. 9, by conducting in FE analyses parametric in the thermal parameters under investigations and by fitting the sampled points of the domain using third-order polynomial functions.

5. Results and discussion

5.1. *Parameters calibration and fitting robustness*

Figure 10a and b show the 3D plot of the square residual sum $\varepsilon_{w,h}$ and ε_{Rq} as a function of the 2D thermal parameters λ_x and λ_y. Similarly, Figure 10c and d show the 3D plot of the same residuals vs. the 3D thermal parameters λ and z_{laser}. Looking at Fig. 10a, it can be noted that calibrating the 2D thermal model (AETC2D) using the melt pool size measurements results in a clear identification of the optimal thermal parameters, viz. $\lambda_x=8$ and $\lambda_z=16$, as the objective

function displays a unique minimum in the explored domain of the parameters. When the same model is calibrated using the roughness measurement, the resulting objective function displays a much less marked global minimum, which, if on one side is sufficiently responsive towards decreasing values of λ_x, on the other one is little sensitive to changes in the parameter λ_z. As a result, the optimal value of λ_x ($\lambda_x=7$) is in good agreement with that found with the previous approach, whereas the estimation of λ_z ($\lambda_z=12$) seems to deviate to a larger extent from the former one.

The calibration of the 3D thermal model (IETC3D) offers a similar scenario. The objective function built starting from the melt pool size measurement displays a unique global minimum (located at $\lambda_x=4$ and $z_{laser}=60$ μm) with a steep gradient along the z_{laser} axis and a much less pronounced effect of the augmentation factor λ_x. The same objective function obtained from the roughness measurements has a complicated shape, with the global minimum (located at $\lambda_x=4$ and $z_{laser}=80$ μm) strongly deviating from the fitting curve. On the other hand, the parameters corresponding to this minimum are close to those estimated by the former approach. To conclude, it is worth noticing that calibrating IETC3D using two different sets of measurements (viz. melt pool size and roughness) leads to more coherent results than calibrating AETC2D with the same approach.

To check the robustness of such calibration methods, a Monte Carlo analysis has been carried out as described in Section 4.5. Figure 11a and b illustrates the coordinates of the minima of the objective functions for the 1000 trials carried out for the AETC2D and IETC3D approaches, respectively. Looking at Fig. 11a, it can be noted that the points are clustered around the optimal points shown in Fig. 10a and b. However, despite the above discussed shape of the objective function, the points are less scattered when the model is calibrated using roughness instead of melt pool size measurements. Figure 11b depicts a similar scenario: the points are clustered around the minima found by minimizing Eq. (6) and (7). The calibration based on melt pool size measures clearly indicates in 60 μm the optimal laser penetration depth z_{laser}, whereas that based on roughness shows the majority of optimal points scattered between 60 and 80 μm. Both calibration approaches seem to indicate an optimal augmentation factor λ comprised between 4 and 6.

5.2. *Numerical estimations of melt pool size and roughness*

In this section, we will discuss the capability of AETC2D and IETC3D approaches to predict melt pool size and measurement. For the sake of brevity, we will consider the outcomes of the models calibrated using melt pool size measurements, only. Similar considerations hold for the models calibrated using roughness estimations.

In Fig. 12, the effect of each L-PBF machine process parameter on roughness is assessed separately, comparing the experimental with the numerical results. It is notable that, an increment of *point distance* tends to increase the roughness, since, when laser spots are more spaced apart, the energy density is less and, thus, the cohesion between the adjacent weld tracks is less effective. The opposite occurs for increasing *time exposure.* Indeed, longer dwell-times of

the laser spot will result in more intense thermal energy input. The roughness decreases by increasing the laser power up to plateau above 450W. These trends seem to be well predicted by the numerical approaches, especially IETC3D. Intuitively, observing the plot Fig. 12d, a high energy density tends to decrease the roughness, since the energy input is high enough to widely and homogenously spread the liquid metal. Furthermore, the deviation from the outlined trend of the data would suggest that roughness-to-energy-density dependency is quite complex and, thus, some synergy among other process parameters could exist. Once again, this complex trend is well described by both FE approaches, in particular IETC3D.

In Fig. 13, experimental width, height and roughness are compared with those predicted by both calibrated models. It can be noted that the 3D approach (IETC3D) allows for a better estimation of width and height of the melt pool with respect to the 2D (AETC2D) method in the majority of the 27 DoE experiments analysed in this paper. This clearly reflects the better accuracy of the same approach also in the estimation of the roughness.

Despite the evident success of the present numerical model in assessing the roughness, it has to be made clear that the present approach relies on a gross approximation, namely that the surface morphology can be estimated from the thermal behaviour of a single laser scan. In reality, the surface morphology is the result of multiple laser scans, whereby the material undergoes repeated fusion and solidification processes at each laser scan. The thermal interaction between adjacent weld seams is clearly not captured in the present work, which is based on the simulation of a single laser scan. Interestingly, by tuning the thermal parameters of the FE model it is possible to artificially account for the effect of multiple laser scans on the final roughness, but at the cost of worsening the simulation of the thermal behaviour of the melt pool produced by the single laser scan. The issue of improving the estimation of the surface morphology by numerically modelling the interaction of adjacent melt pools will be matter of future investigations.

To conclude the results discussion, it is possible to affirm that a satisfactory estimation of the thermal behaviour of the melt pool produced by a single laser scan can be obtained from a numerical model, in which both powder and liquid states are modelled as continua and all the involved heat transfer modes are lumped into equivalent heat conduction. This necessitates the calibration of the equivalent powder conductivity and the laser penetration depth through measurements of the size of the weld seam. The thermal parameters are highly sensitive to the uncertainty in the experimental data used for their calibration and this demonstrates the necessity of a large number of experiments to achieve a reasonable robustness. The 3D approach yields more accurate estimations of melt pool size and roughness and is less sensitive to experimental uncertainties in the melt pool size and seems therefore to be more effective than the 2D approach. Finally, the size of the melt pool produced by a single scan can be used for a first approximate estimation of the roughness produced by successive laser scans.

6. Conclusions

A FE model of L-PBF Ti6Al4V has been developed and calibrated by introducing enhanced thermal conductivity model only above the melting temperature. For sake of computational lightness, all the bodies including the powder have been modelled as continuous media. The phase transitions as well as the irreversible transformation powder-to-solid are modelled. A scan-line composed by 15 laser spots is simulated in order to have an estimation of the melting pool size and its behaviour. Initially, the laser interaction has been considered as shallow heat flux applied on the top surface of the powder bed. Thermal properties have been fine-tuned in order to calibrate the model on the basis of empirical results. In particular, thermal conductivity over the melting temperature is increased by a factor λ (*enhanced thermal conductivity*) to consider, in a simplified manner, complicated heat transfer phenomena. For this purpose, two main approaches have been used. The first one is based on an *anisotropic enhanced thermal conductivity* with laser interaction modelled as an imposed surface heat flux (AETC2D). The second one consists in introducing *isotropic enhanced thermal conductivity* and modelling the laser interaction as a volumetric heat generated, whose depth is calibrated along with the enhancement factor (IETC3D).

The followings are the key conclusions that can be drawn from this study:

- Experimental measurements indicate a correlation between melt pool dimensions (width and height) and roughness Rq. Therefore, the size of the melt pool produced by a single scan can be used for a first approximate estimation of the roughness produced by successive laser scans.

- The thermal parameters of the FE models can be calibrated on the base of melt pool size or roughness measurements. In any case, a large number of DoE experiment is necessary to achieve an adequate robustness against experimental uncertainties.

- The 3D approach (IETC3D) yields more accurate estimations of melt pool size and roughness and is less sensitive to experimental uncertainties in the melt pool size and seems therefore to be more effective than the 2D approach (AETC2D).

References

[1] Gibson I, Rosen D, Stucker B 2015 Additive manufacturing technologies (New York: Springer-Verlag)

[2] Vandenbroucke B, Kruth J-P (2007) Selective laser melting of biocompatible metals for rapid manufacturing of medical parts. Rapid Prototyp J 13(4):196–203. https://www.doi.org/10.1108/13552540710776142

[3] Yadroitsev I, Smurov I (2011) Surface morphology in selective laser melting of metal powders. Phys Proc 12:264–270. https://www.doi.org/10.1016/j.phpro.2011.03.034

[4] Yasa E, Kruth J-P (2011) Application of laser re-melting on selective laser melting parts. Adv Prod Eng Manag 6(4):259–270. http://apem-journal.org/Archives/2011/APEM6-4_259-270.pdf

[5] Matthias M, Körner C (2016) Multiscale Modeling of Powder Bed–Based Additive Manufacturing. Annual Review of Materials Research 46:1, 93-123 https://doi.org/10.1146/annurev-matsci-070115-032158

[6] Mercelis P, Kruth JP (2006) Residual stresses in selective laser sintering and selective laser melting. Rapid Prototyp J 12(5):254–265. https://www.doi.org/10.1108/13552540610707013

[7] Benedetti M, Torresani E, Leoni M, Fontanari V, Bandini M, Pederzolli C, Potrich C (2017) The effect of post-sintering treatments on the fatigue and biological behavior of Ti-6Al-4V ELI parts made by selective laser melting. Journal of the mechanical behavior of biomedical materials 71:295–306.

[8] Benedetti M, Fontanari V, Bandini M, Zanini F, Carmignato S (2018) Low- and high-cycle fatigue resistance of Ti-6Al-4V ELI additively manufactured via selective laser melting: Mean stress and defect sensitivity. International Journal of Fatigue, 107:96-109.

[9] Roberts R I.A., Wang C.J., Esterlein R., Stanford M., Mynors D.J. (2009) A three-dimensional finite element analysis of the temperature field during laser melting of metal powders in additive layer manufacturing, International Journal of Machine Tools and Manufacture, 49(12–13): 916-923, ISSN 0890-6955,https://doi.org/10.1016/j.ijmachtools.2009.07.004.

[10] Hodge NE, Ferencz RM, Solberg JM (2014) Implementation of a thermomechanical model for the simulation of selective laser melting. Comput Mech 54(1):33–51. https://doi.org/10.1007/s00466-014-1024-2.

[11] Nikoukar M, Patil N, Pal D, Stucker B (2013) Methods for enhancing the speed of numerical calculations for the prediction of the mechanical behavior of parts made using additive manufacturing. International solid freeform fabrication symposium, Austin, Texas, USA. http://sffsymposium.engr.utexas.edu/Manuscripts/2013/2013-42-Nikoukar.pdf

[12] Patil N, Pal D, Stucker B (2013) A new finite element solver using numerical eigen modes for fast simulation of additive manufacturing processes. International solid freeform fabrication symposium, Austin, Texas, USA. https://pdfs.semanticscholar.org/8388/ffff4a5e06f2b23c534b4b115c584e1d556e.pdf.

[13] Zeng D, Pal D, Patil N, Stucker B (2013) A new dynamic mesh method applied to the simulation of selective laser melting. International solid freeform fabrication symposium, Austin, Texas, USA. http://sffsymposium.engr.utexas.edu/Manuscripts/2013/2013-44-Zeng.pdf.

[14] de La Batut B., Fergani O., Brotan V., Bambach M., El Mansouri M. (2017) Analytical and Numerical Temperature Prediction in Direct Metal Deposition of Ti6Al4V. Journal of Manufacturing and Materials Processing 1(1), 3. https://doi.org/10.3390/jmmp1010003.

[15] Fergani O., Berto F., Welo T., Liang S.Y. (2016) Analytical modelling of residual stress in additive manufacturing. Fatigue & fracture of Engineering Materials & Structures, 40(6):971-978. https://doi.org/10.1111/ffe.12560

[16] Papadakis L, Loizou A, Risse J (2014) A computational reduction model for appraising structural effects in selective laser melting manufacturing. Virtual Phys Prototyp 9(1):17–25. https://doi.org/10.1080/17452759.2013.868005.

[17] Denlinger ER, Irwin J, Michaleris P (2014) Thermomechanical Modeling of Additive Manufacturing Large Parts. ASME. *J. Manuf. Sci. Eng*;136(6):061007-061007-8. https://doi.org/10.1115/1.4028669.

[18] Stathatos E, Vosniakos GC (2017) A computationally efficient universal platform for thermal numerical modeling of laser-based additive manufacturing. Proceedings of the Institution of Mechanical Engineers, Part C: Journal of Mechanical Engineering Science, 232(13):2317–2333. https://doi.org/10.1177/0954406217720230

[19] Hu J, Dang D, Shen H, Zhang Z (2012) A finite element model using multi-layered shell element in laser forming, Optics & Laser Technology, 44(4):1148-1155, ISSN 0030-3992, https://doi.org/10.1016/j.optlastec.2011.09.028

[20] Khairallah SA, Anderson A (2014) Mesoscopic simulation model of selective laser melting of stainless steel powder, Journal of Materials Processing Technology, 214(11):2627-2636, ISSN 0924-0136, https://doi.org/10.1016/j.jmatprotec.2014.06.001.

[21] Ganeriwala R., Zohdi T.I (2016) A coupled discrete element-finite difference model of selective laser sintering. Granular Matter 18:21. https://doi.org/10.1007/s10035-016-0626-0

[22] Yang Y.P., Jamshidinia M., Boulware P., Kelly S. M (2018) Prediction of microstructure, residual stress, and deformation in laser powder bed fusion process. Comput Mech 61:599-615. https://doi.org/10.1007/s00466-017-1528-7

[23] Paradis P.F., Ishikawa T. (2005) Surface tension and viscosity measurements of liquid and undercooled alumina by containerless techniques, Jpn. Soc. Appl. Phys. 44:5082–5085. https://doi.org/10.1143/JJAP.44.5082

[24] Safdar S, Pinkerton AJ, Li L, Sheikh MA, Withers PJ (2013) An anisotropic enhanced thermal conductivity approach for modelling laser melt pools for Ni-base super alloys. Appl Math Model 37(3):1187–1195

[25] Safdar S, Pinkerton AJ, Moat R, Li L, Sheikh MA, Preuss M, Withers PJ (2018) An anisotropic enhanced thermal conductivity approach for modelling laser melt pools. Journal of Laser Application, ICALEO 2007, 1305; https://doi.org/10.2351/1.5061002

[26] Ali H., Ghadbeigi H., Mumtaz K (2018) Residual stress development in selective laser-melted Ti6Al4V: a parametric thermal modelling approach. Int J Adv Manuf Technol, 97(5-8): 2621-2633. https://doi.org/10.1007/s00170-018-2104-9

[27] Rosenthal, D. (1946) The theory of moving sources of heat and its application to metal treatments, ASME.

[28] Eagar, T. and Tsai, N. (1983) Temperature fields produced by traveling distributed heat sources. Welding Journal, 62;346-355.

[29] Goldak J., Bibby M., Chakravarti A. (1985) A double ellipsoid finite element model for welding heat sources, International Institute of Welding, 15(2): 299–305.

[30] Criales L.E., Arısoy Y.M., Özel T. (2015) A Sensitivity Analysis Study on the Material Properties and Process Parameters for Selective Laser Melting of Inconel 625, in ASME 2015 International Manufacturing Science and Engineering Conference, American Society of Mechanical Engineers, pp. V001T02A062-V001T02A062.

[31] Fu C., Guo Y. (2014) 3-Dimensional Finite Element Modeling of Selective Laser Melting Ti-6 Al-4 V Alloy, in Solid Freeform Fabrication Symposium 2014 Proceedings. http://sffsymposium.engr.utexas.edu/sites/default/files/2014-089-Fu.pdf

[32] Gu D, He B (2016) Finite element simulation and experimental investigation of residual stresses in selective laser melted Ti–Ni shape memory alloy, Computational Materials Science, 117:221-232, ISSN 0927-0256, https://doi.org/10.1016/j.commatsci.2016.01.044.

[33] Huang Y., Yang L.J., Du X.Z., Yang Y.P. (2016) Finite element analysis of thermal behavior of metal powder during selective laser melting, International Journal of Thermal Sciences, 104:146-157, ISSN 1290-0729, https://doi.org/10.1016/j.ijthermalsci.2016.01.007.

[34] Loh LE, Chua CK, Yeong WY, Song J, Mapar M, Sing SL, Liu ZH, Zhang DQ (2015) Numerical investigation and an effective modelling on the Selective Laser Melting (L-PBF) process with aluminium

alloy 6061, International Journal of Heat and Mass Transfer, 80:288-300, ISSN 0017-9310, https://doi.org/10.1016/j.ijheatmasstransfer.2014.09.014.

[35] Masmoudi A, Bolot R, Coddet C (2015) Investigation of the laser–powder–atmosphere interaction zone during the selective laser melting process, Journal of Materials Processing Technology, 225:122-132, ISSN 0924-0136, https://doi.org/10.1016/j.jmatprotec.2015.05.008.

[36] Liu C., Wu B., Zhang J.X (2010) Numerical investigation of residual stress in thick titanium alloy plate joined with electron beam welding. Metall and Materi Trans B, 41:1129-1138. https://doi.org/10.1007/s11663-010-9408-y.

[37] Bai J., Goodridge R.D., Yuan S., Zhou K., Chua C.K., Wei J. (2015) Thermal Influence of CNT on the Polyamide 12 Nanocomposite for Selective Laser Sintering. Molecules, 20(10):19041-50. https://doi.org/10.3390/molecules201019041.

[38] Raghavan N, Dehoff R, Pannala S, Simunovic S, Kirka M, Turner J, Carlson N, Babu SS (2016) Numerical modeling of heat-transfer and the influence of process parameters on tailoring the grain morphology of IN718 in electron beam additive manufacturing, Acta Materialia, 112:303-314, ISSN 1359-6454, https://doi.org/10.1016/j.actamat.2016.03.063.

[39] Romano J, Ladani L, Razmi J, Sadowski M (2015) Temperature distribution and melt geometry in laser and electron-beam melting processes – A comparison among common materials. Additive Manufacturing, 8:1-11, ISSN 2214-8604, https://doi.org/10.1016/j.addma.2015.07.003.

[40] Zäh M., Lutzmann S., Kahnert M., Walchshäusl F. (2008) Determination of Process Parameters for Electron Beam Sintering (EBS), in Excerpt from the Proceedings of the COMSOL Conference Hannover. https://www.comsol.it/paper/determination-of-process-parameters-for-electron-beam-sintering-ebs-5049

[41] Fischer P., Karapatis N., Romano V., Glardon R., Weber HP (2002) A model for the interaction of near-infrared laser pulses with metal powders in selective laser sintering Appl Phys A, 74:467-474. https://doi.org/10.1007/s003390101139.

[42] Leach R K (2013) Characterisation of areal surface texture (Heidelberg: Springer Verlag). https://doi.org/10.1007/978-3-642-36458-7

[43] Simonelli M, Tuck C, Aboulkhair N T, Maskery I, Ashcroft I, Wildman R D, Hague R (2015) A study on the laser spatter and the oxidation reactions during selective laser melting of 316L stainless steel, Al-Si10-Mg, and Ti-6Al-4V Metallur. Mater. Trans. A, 46:3842-51. https://doi.org/10.1007/s11661-015-2882-8.

[44] Khairallah SA, Anderson AT, Rubenchik A, King WE (2016) Laser powder-bed fusion additive manufacturing: Physics of complex melt flow and formation mechanisms of pores, spatter, and denudation zones, Acta Materialia, Volume 108:36-45, ISSN 1359-6454, https://doi.org/10.1016/j.actamat.2016.02.014.

[45] Senin N, Thompson A, Leach R (2017) Feature-based characterisation of signature topography in laser powder bed fusion of metals. Measurement Science and Technology, 29(4):045009. https://doi.org/10.1088/1361-6501/aa9e19.

[46] ISO 4287:1997. Geometrical product specifications (GPS) - Surface texture: Profile method – terms, definitions and surface texture parameters.

[47] ISO 13565-1:1996: Geometrical product specifications (GPS) – Surface texture: Profile method; Surfaces having stratified functional properties – Part 1: Filtering and general measurement conditions.

[48] V.A. Vinokurov (1977) Welding Stresses and Distortion: Determination and Elimination. 1st ed. British Library Lending Division; 317 DOI: 9780853501664

[49] D. Hu, R. Kovacevic (2003) Modelling and measuring the thermal behaviour of the molten pool in closed-loop controlled laser-based additive manufacturing. Proceedings of the Institution of Mechanical Engineers, Part B: Journal of Engineering Manufacture;. 217(4):441-452. DOI: https://doi.org/10.1243/095440503321628125.

[50] Boyer R., Collings E.W., Welsch G. (1994) Materials Properties Handbook: Titanium Alloys. ASM International.

[51] Boivineau M., Cagran C., Doytier D., Eyraud V., Nadal M. -H., Whiltan B., Plottlacher G. (2006) Thermophysical Properties of Solid and Liquid Ti-6Al-4V (TA6V) Alloy. International Journal of Thermophysics.; 27(2):507-529. https://doi.org/10.1007/PL00021868.

[52] Zhang Y, Chen Q, Guillemot G, Gandin CA, Bellet M (2018) Numerical modelling of fluid and solid thermomechanics in additive manufacturing by powder-bed fusion: Continuum and level set formulation applied to track- and part-scale simulations, Comptes Rendus Mécanique, 346(11):1055-1071, https://doi.org/10.1016/j.crme.2018.08.008.
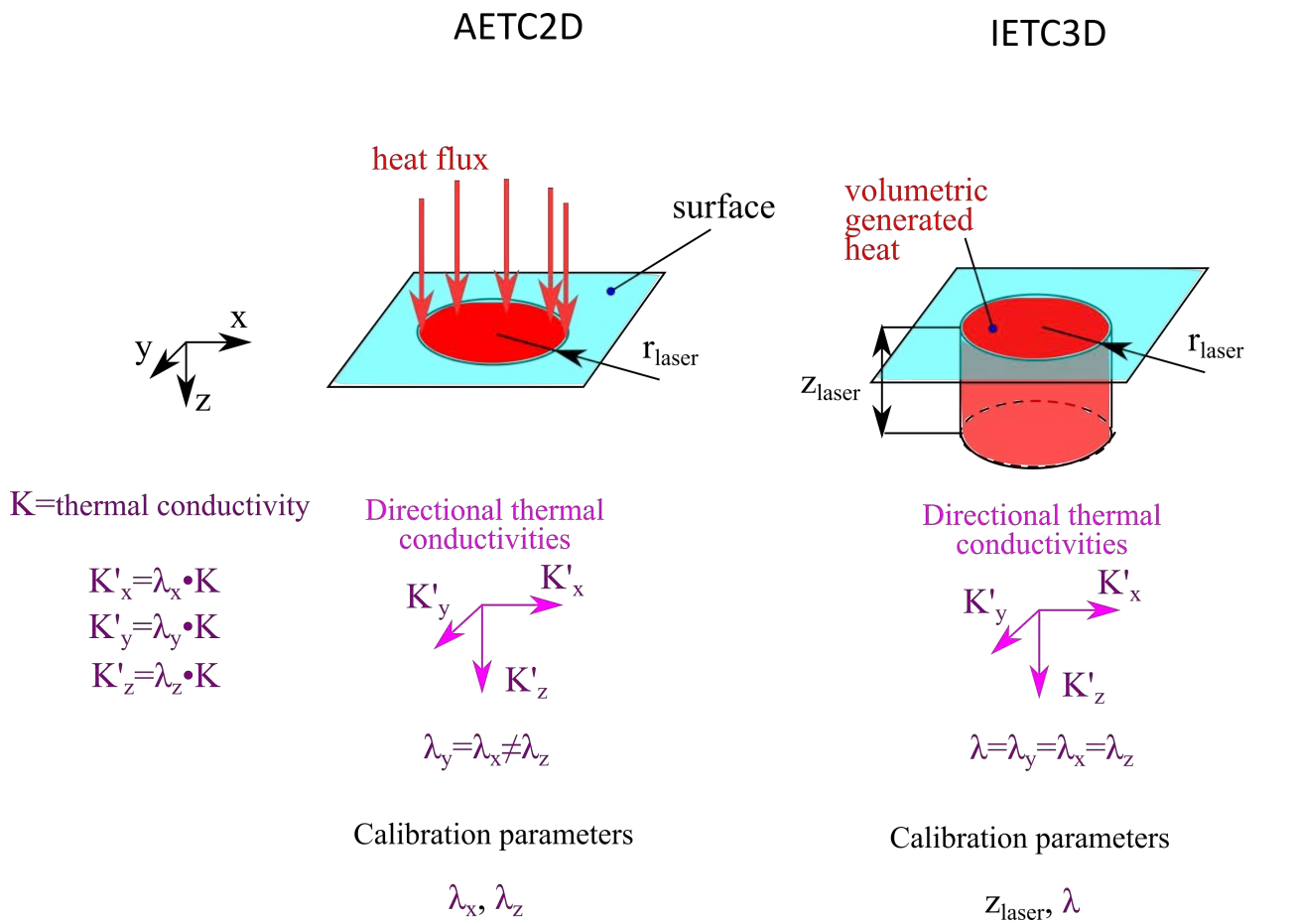
Figures

Fig. 1. Schematic illustration of the two modelling approaches "Anisotropic Enhanced Thermal Conductivity 2D" (AETC2D) and "Isotropic Enhanced Thermal Conductivity 3D" (IETC3D). In the first one, the laser irradiance is modelled as a surface heat flux in the laser spot of radius r_{laser}, whereas, in the second one, as a volumetric heat generated in a cylindrical volume having the same radius and a certain depth z_{laser}. Thermal conductivities along x, y and z obtained by multiplying the initial thermal conductivity K with λ factors, but only over the melting temperature. For AETC2D, thermal conductivity of liquid is assumed anisotropic and, thus, the calibration parameters are λ_x and λ_z. Conversely, for IETC3D, thermal conductivity of liquid is assumed isotropic and, thus, the calibration parameters are λ_x and z_{laser}.
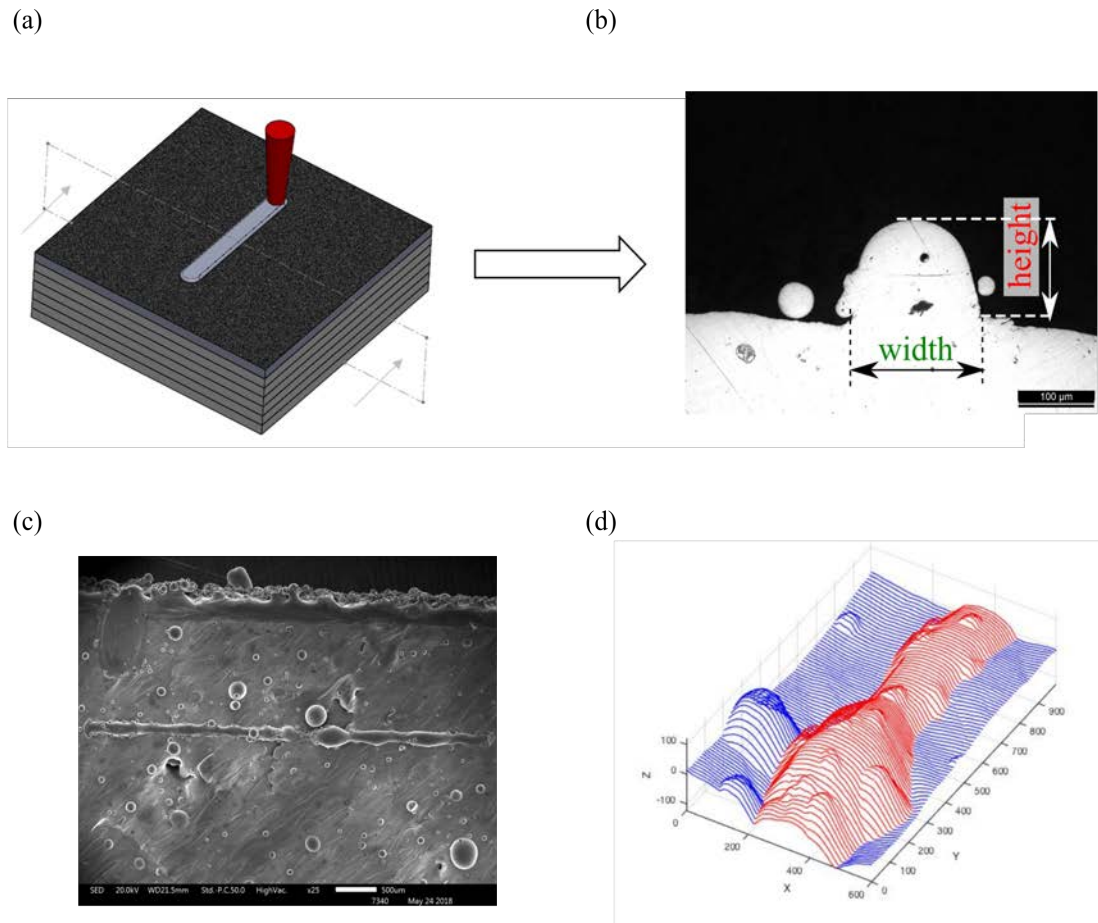
Fig. 2. Single laser scanning (a) are performed for each combination of process parameters listed in Tab. 5. (b) cross section of a seam, whose height and width are used to validate the model. (c) Top view SEM photos are analysed by image analyser functions in MatLab (watershed) in order to measure seam cross section width. (d) 3D profile of each seam is processed to measure its height (red area).
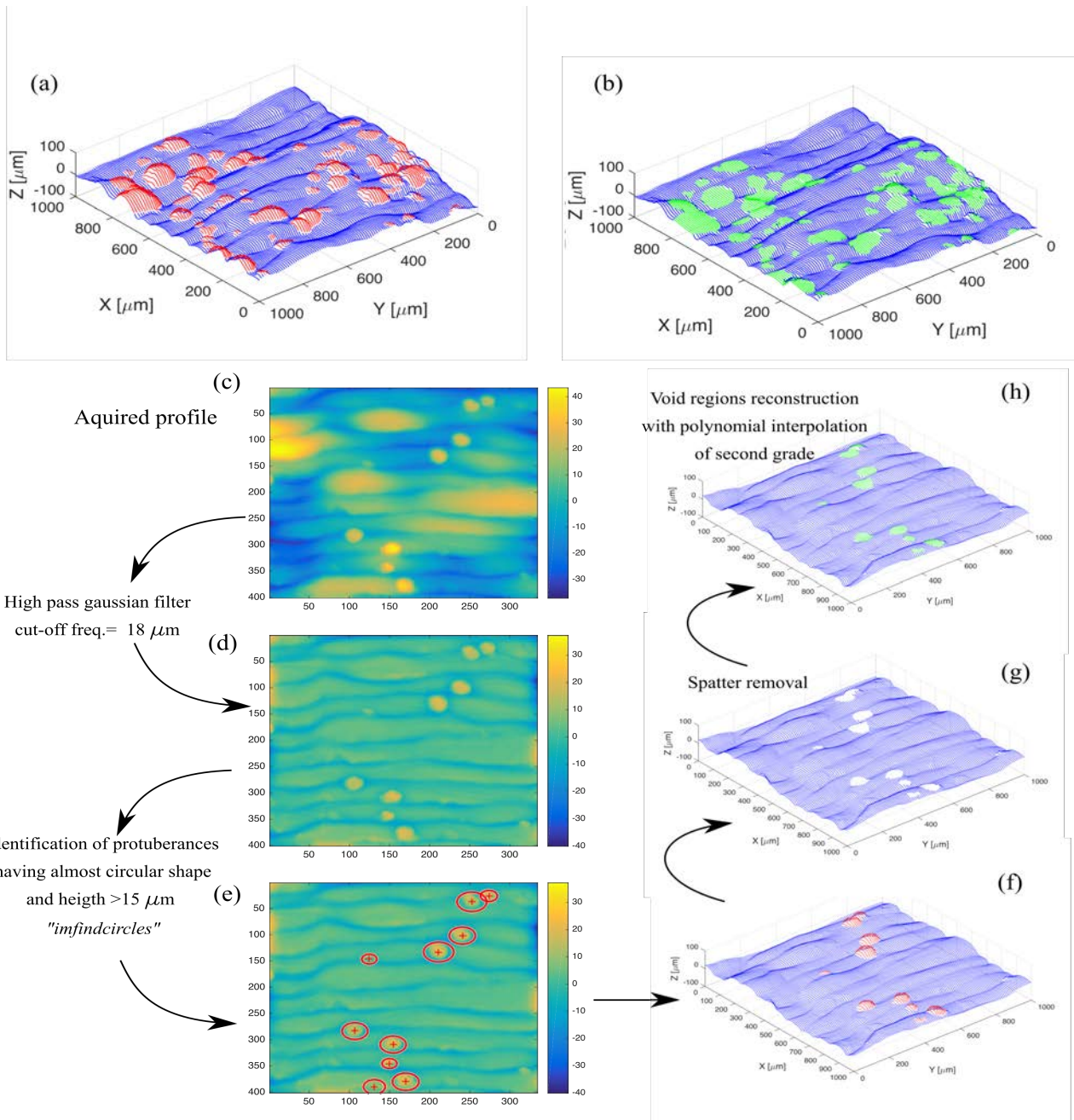
Fig. 3. 3D profile of upper surface of printed samples (mechanical profiler). (a) original surface, spatter identification is showed in red; (b) surface "cleaned", the spatters are removed and the void region are reconstructed via polynomial interpolation (green region). The diagram of the spatter identification algorithm is also shown. The profile (c) is initially filtered with a Gaussian filter cut-off frequency of18μm so as to distinguish the spatters with respect to the surrounding waviness of the surface (d). The protrusions higher than 15μm and having almost circular shape are identified as spatters. Circular shape is checked by the function "imfindcircles" in Matlab (e)(f). Then the spatters are removed (g) and substituted by surfaces reconstructed by polynomial interpolation (h). As a result, a smoothed surface without spatters is obtained.
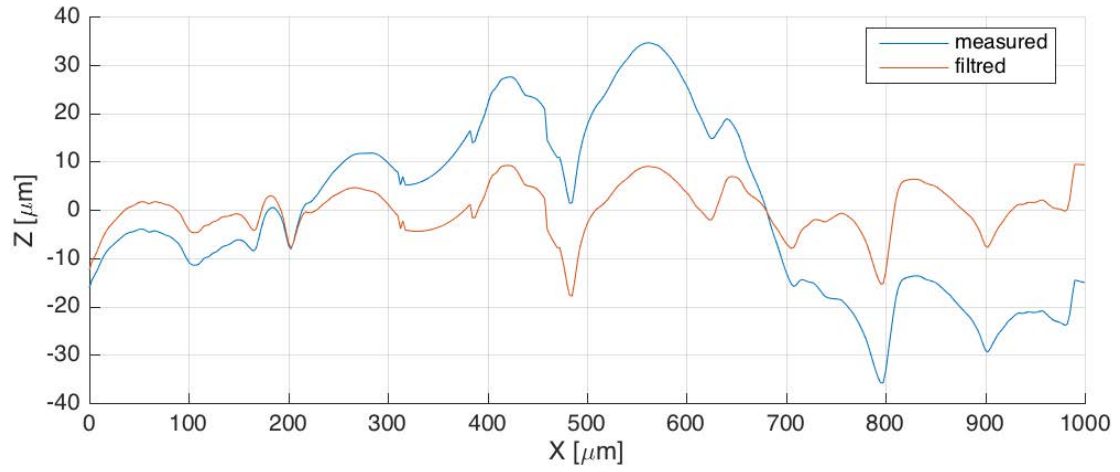
Fig. 4. The smoothed surface profile (without spatters) is filtered again using the same Gaussian filter with cut-off 8 µm in order to identify the waviness of the overlapped tracks neglecting the macro-irregularities.
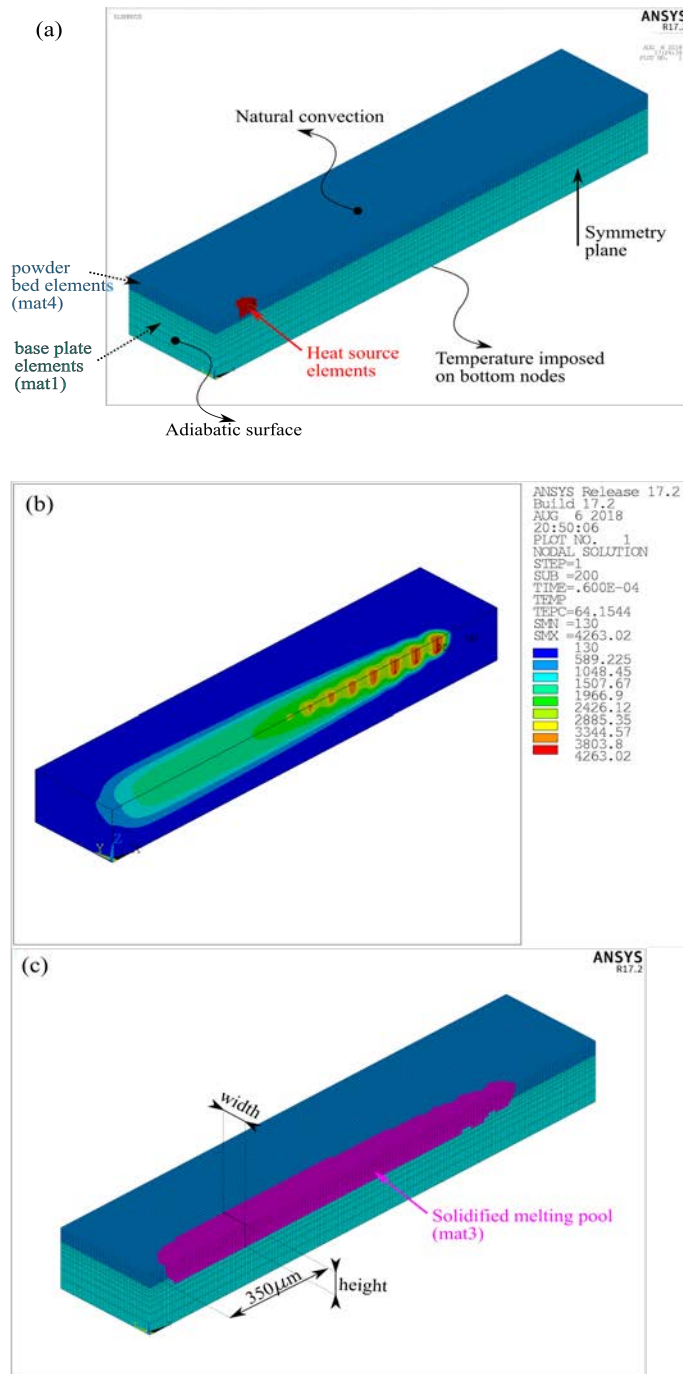
Fig. 5. FE model. (a) Boundary conditions. (b) Temperature distribution after a laser scanning. (c) post processing. The magenta elements represent solidified melting pool. Width and height of melting pool are measured at the cross-section 350 μm away from the right edge.
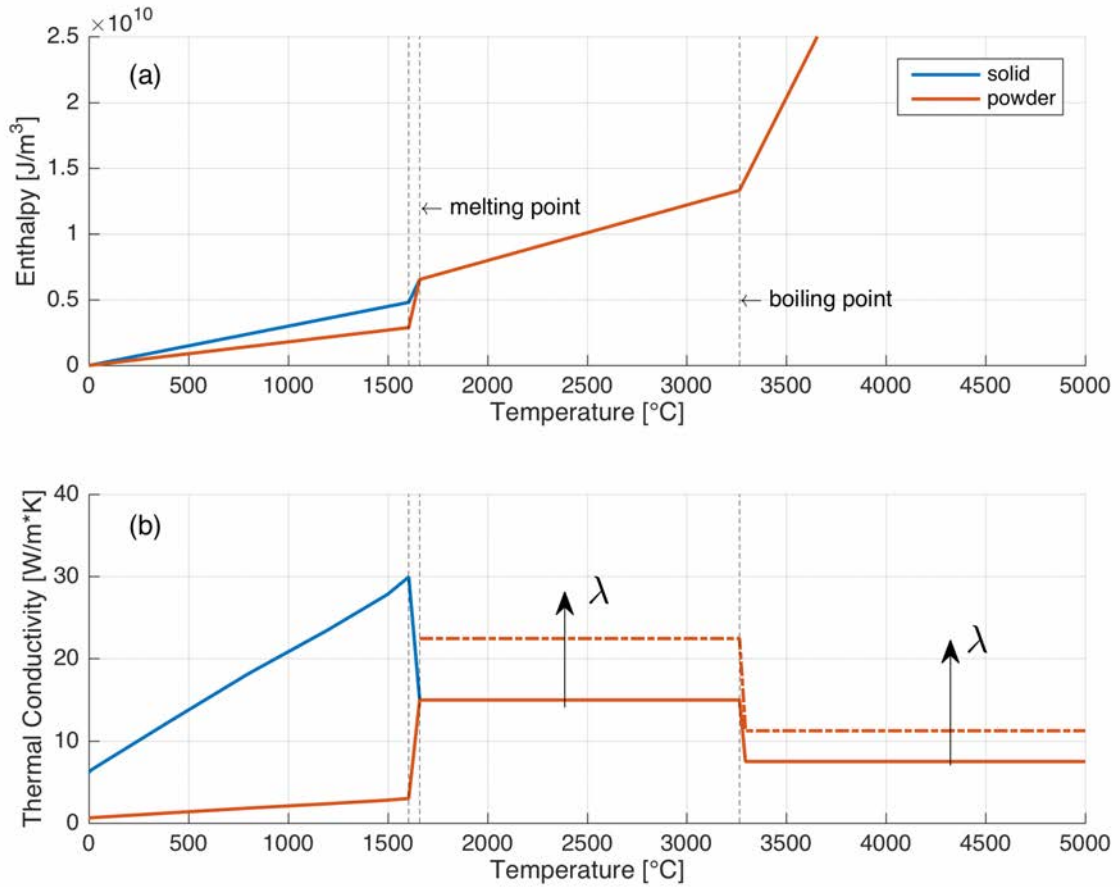
Fig. 6. Material properties in the FEM: enthalpy (a) and thermal conductivity (b). Thermal conductivity above the melting point is multiplied by the factor λ.

$$R_q = \sqrt{\frac{1}{l}\int_0^l Z^2(x)\,dx}$$
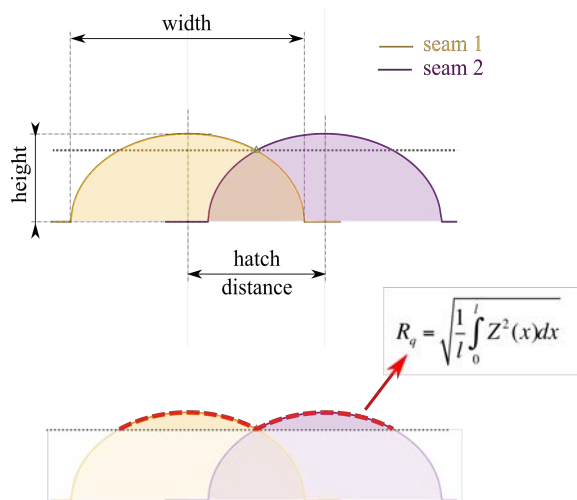
Fig. 7. Criterion for estimating roughness starting from width, height and hatch distance predicted by FE model.
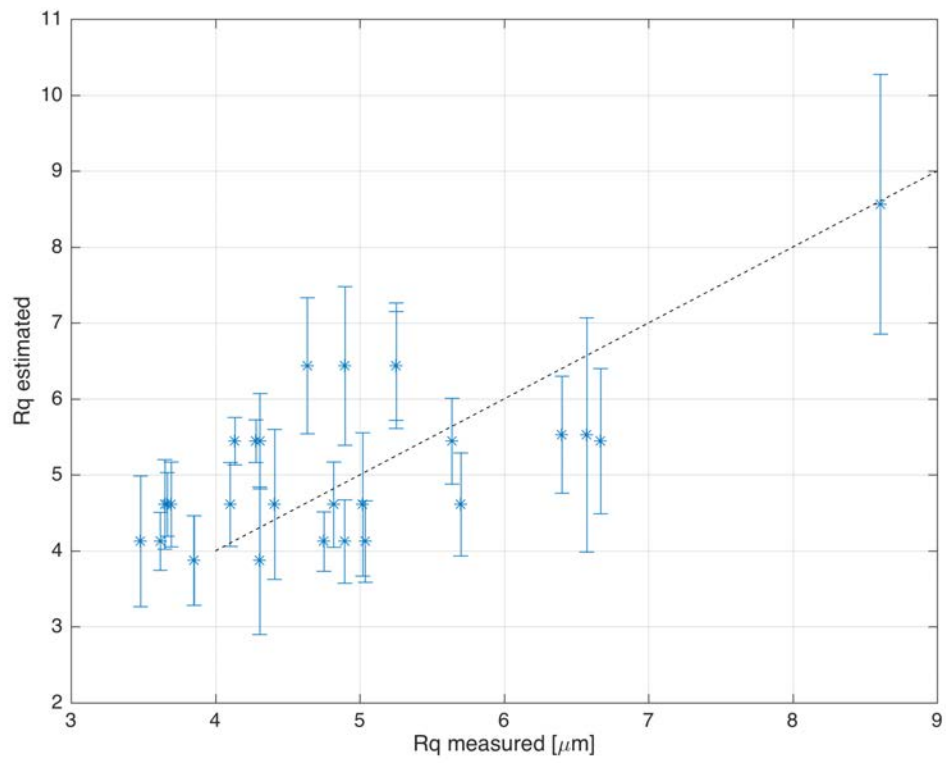
Fig. 8. Rq estimated from experimental measurements of melt pool width and height vs. experimental measures.
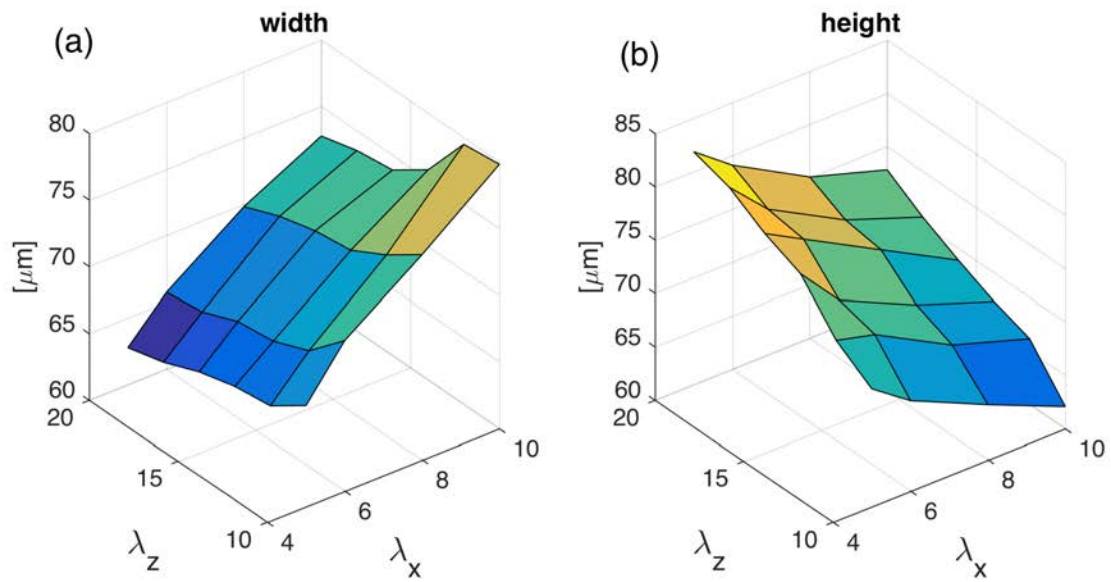
Fig. 9. Influence of augmentation factors λ on width and height of melting pool.
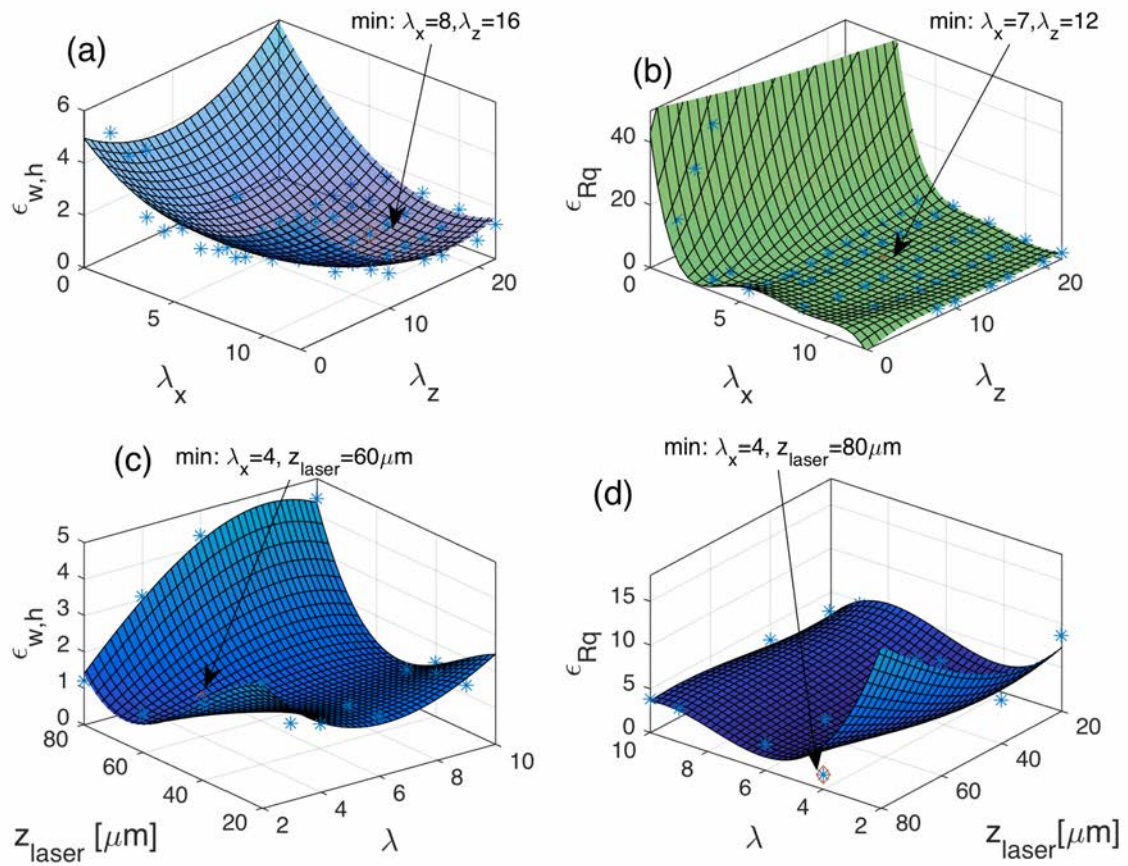
Fig. 10. Variation of the objective functions $\varepsilon_{w,h}$ (a) and ε_{Rq} (b) as a function of the thermal parameters λ_x, λ_z, for AETC2D model and λ and z_{laser}, for the IETC3D model.
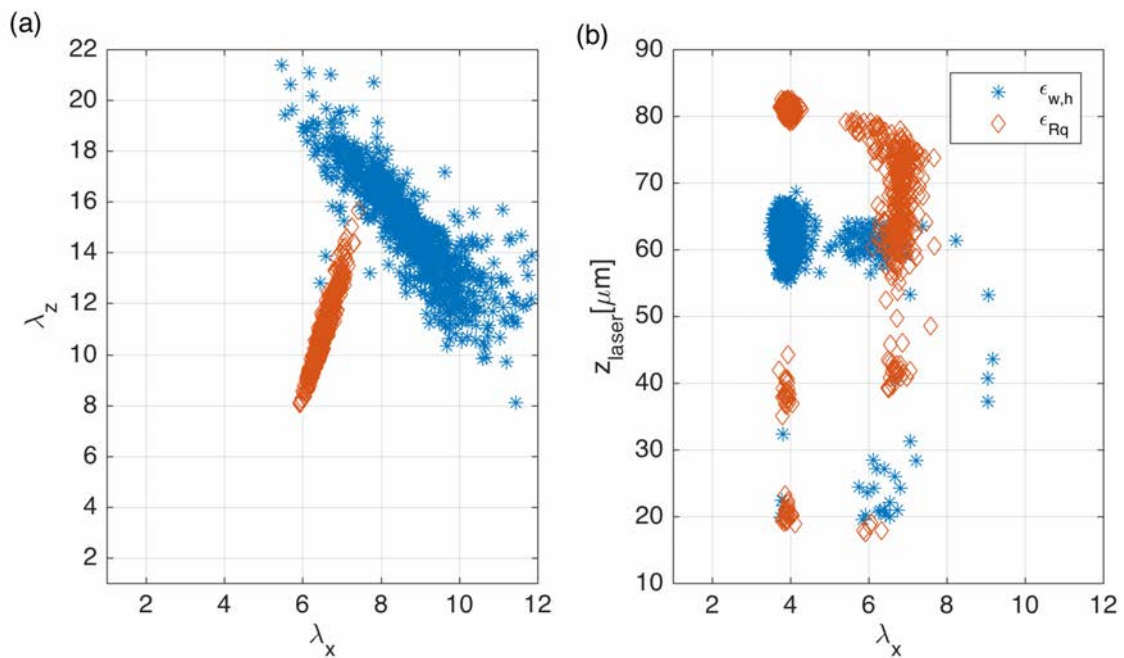
Fig. 11. Results of 1000 Monte Carlo simulations carried out to investigate the uncertainty in the estimation of the optimal parameters of (a) AETC2D and (b) IETC3D approaches. Blue stars and orange diamonds represent points found by minimization of $\varepsilon_{w,h}$ and ε_{Rq}, respectively.
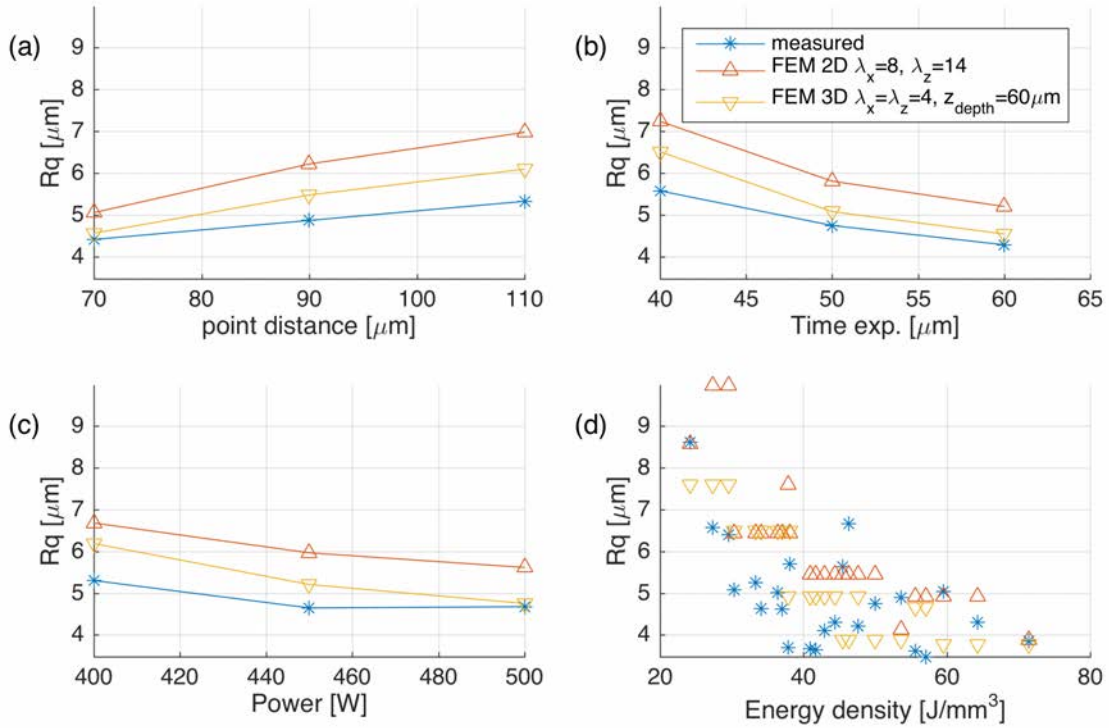

Fig. 12. The effect of each L-PBF machine process parameter is assessed separately, comparing the empirical results with those of the calibrated models IETC3D and AETC2D. Roughness is plotted vs. (a) point distance (b) time exposure (c) power and (d) Energy density.
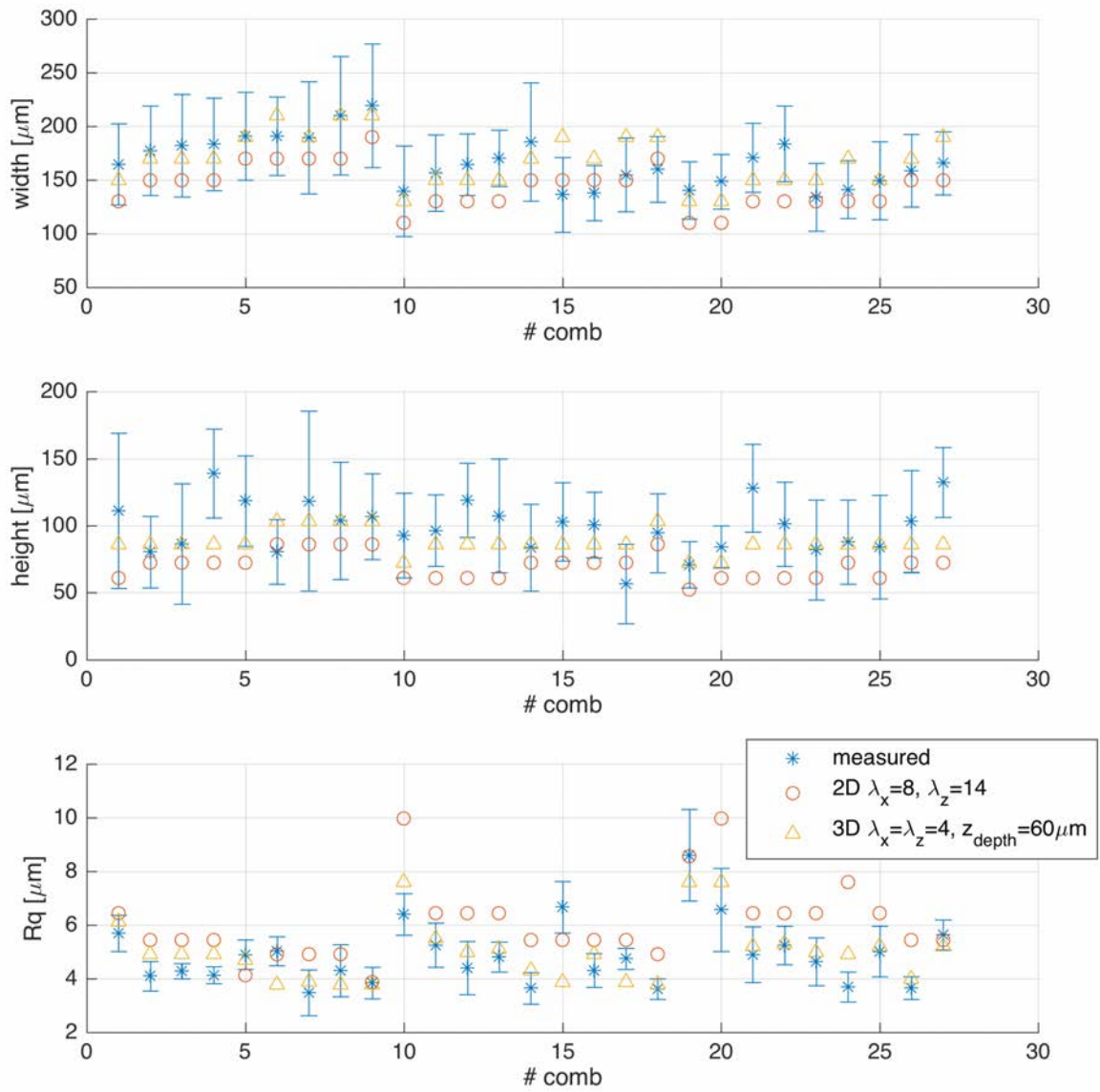
Fig. 13. Comparison between experimental width, height and roughness and those predicted by both the calibrated models IETC3D and AETC2D for each combination of process parameters.